Title: A mechanistic erosion model for cosmogenic nuclide inheritance in fluvial single-clast exposure ages

Veronica B. Prush[a,*], Michael E. Oskin[a]

[a]Department of Earth and Planetary Sciences
University of California, Davis
1 Shields Avenue
Davis, CA 95616
United States

*Corresponding Author

Prush Contact Information:
vbprush@ucdavis.edu

Oskin Contact Information:
meoskin@ucdavis.edu

Abstract

Terrestrial cosmogenic nuclides (TCNs), produced by the bombardment of Earth's surface by cosmic rays, are widely used for age-dating and pacing surface processes. Sediments carry an inherited TCN concentration, useful for quantifying erosion and transport rates, but that must be subtracted when age-dating sedimentary landforms, such as alluvial fans. Here we present a mechanistic model of inheritance based on the contributions of episodic erosion by landsliding and steady, background erosion due to soil formation. The balance of these processes, revealed by the distribution of inheritance recorded by a population of individual surface clasts, affects rates of soil generation and the cycling of material through the Earth's critical zone – the surficial layer upon which all terrestrial life depends. We test our inheritance model on alluvial fan TCN datasets drawn from a global compilation of active-fault slip-rate studies. Inheritance-corrected landform ages are systematically younger than published ages. Our results reveal a consistent signature of spatiotemporal clustering of landslides, important for quantifying hazard and for understanding the coupling of physical and chemical erosion. Application of our inheritance model provides a rigorous approach to correcting landform ages for inheritance and reveals information on landslide frequency, with broad implications for hazard and land use.

Keywords: Cosmogenic radionuclides, Erosion, Landslides, generalized Pareto distribution

1. Introduction:

Terrestrial cosmogenic nuclide (TCN) techniques have revolutionized the field of geomorphology by providing a means for constraining landform ages and rates of surface processes over the Quaternary (e.g., Gosse and Phillips, 2001; Lal, 1991). This time period is key to quantifying natural hazard recurrence and modeling land-surface processes relevant to society. Such processes include earthquake hazard models and forecasts, which are underpinned by estimates of fault motion based on age-dating of offset Quaternary deposits (e.g., Page et al., 2014), and calculation of erosion rates, which quantify the stripping and regeneration rates of soil (e.g., Granger and Riebe, 2013).

TCNs are produced during the bombardment of Earth’s surface by cosmic rays. Cosmic rays enter the atmosphere and produce new nuclides by spallation (Cerling and Craig, 1994; Gosse and Phillips, 2001; Lal, 1991). The production rate of TCNs is a function of shielding (for example, by topographic blocking), elevation, atmospheric pressure, and geomagnetic field intensity (Cerling and Craig, 1994; Gosse and Phillips, 2001; Lal, 1991; Lifton et al., 2014; Stone, 2000). Isotopes commonly used in geomorphological applications include Beryllium-10, Aluminum-26, Chlorine-36, Helium-3, and Neon-21. Because TCN production occurs mostly in the upper two meters of Earth's surface (Lal, 1991), TCN concentrations are widely used to track sediment erosion and transport. For surface age-dating applications, TCN concentration acquired during erosion constitutes an added age component, referred to as inheritance, that must be removed (e.g., Anderson et al., 1996).

In eroding landscapes lacking long-term sediment storage, the mean concentration of the TCN Beryllium-10 (^{10}Be) in quartz from well-mixed river sand may be interpreted as a steady erosion rate of the source catchment (Brown et al., 1995; Niemi et al., 2005). However, this model does not account for the episodic nature of erosion processes, in particular by landsliding, shown numerically to strongly bias TCN erosion rate measurements (e.g., Niemi et al., 2005; West et al., 2014; Yanites et al., 2009). Landslides dominate erosion of actively uplifting mountain ranges (Korup et al., 2010). Decadal studies show that extreme events, such as major storms and earthquakes, modulate landslide occurrence (Dadson et al., 2003; McPhillips et al., 2014; West et al., 2014), temporarily increasing sediment yield and solute flux (Emberson et al., 2016; West et al., 2014). Simulations of landslide recurrence predict a patchwork renewal of landscapes (Niemi et al., 2005; Yanites et al., 2009), episodically exposing fresh rock surfaces to weathering. Because chemical weathering and soil production rates decline over time as regolith forms (Gabet, 2007; Taylor and Blum, 1995), the feedback between physical and chemical erosion, critical to understanding coupling of erosion to atmospheric carbon dioxide and organic carbon cycling (Kump et al., 2000), depends on landslide renewal time and its spatial variation. In addition to geomorphic and landscape evolution consequences, quantifying the long-term, catchment-wide recurrence behavior of landslides is essential for mitigating their environmental and hazard consequences.

Here we derive a mechanistic model for the distribution of terrestrial cosmogenic nuclide (TCN) exposure ages within a population of sedimentary clasts, based on balance of landslide frequency and steady, background erosion in the source catchment (Fig. 1). To test the applicability of this model, we analyze 64 clast-age datasets drawn from the literature (Table S1), primarily fault slip-rate studies with exposure age dating applied to alluvial fans and stream terraces. From a population of surface clast ^{10}Be measurements (boulder or cobble), these studies commonly estimate surface age from the mean of the youngest cluster of clast ages, which are assumed to lack inheritance (e.g., Van Der Woerd et al., 2002). However, such clustering is not always apparent, and the filtering and averaging employed assumes clast ages should be normally distributed. We show that inheritance resulting from a combination of steady, background erosion and episodic landslides follows a generalized Pareto distribution. This probabilistic model of clast inheritance permits rigorous assessment of its contribution to sample ages, and generally results in younger landform dates than published. This model also explains the spectrum of observed clast-age distributions, attributable to catchment-scale variations in landslide recurrence and erosion rates.

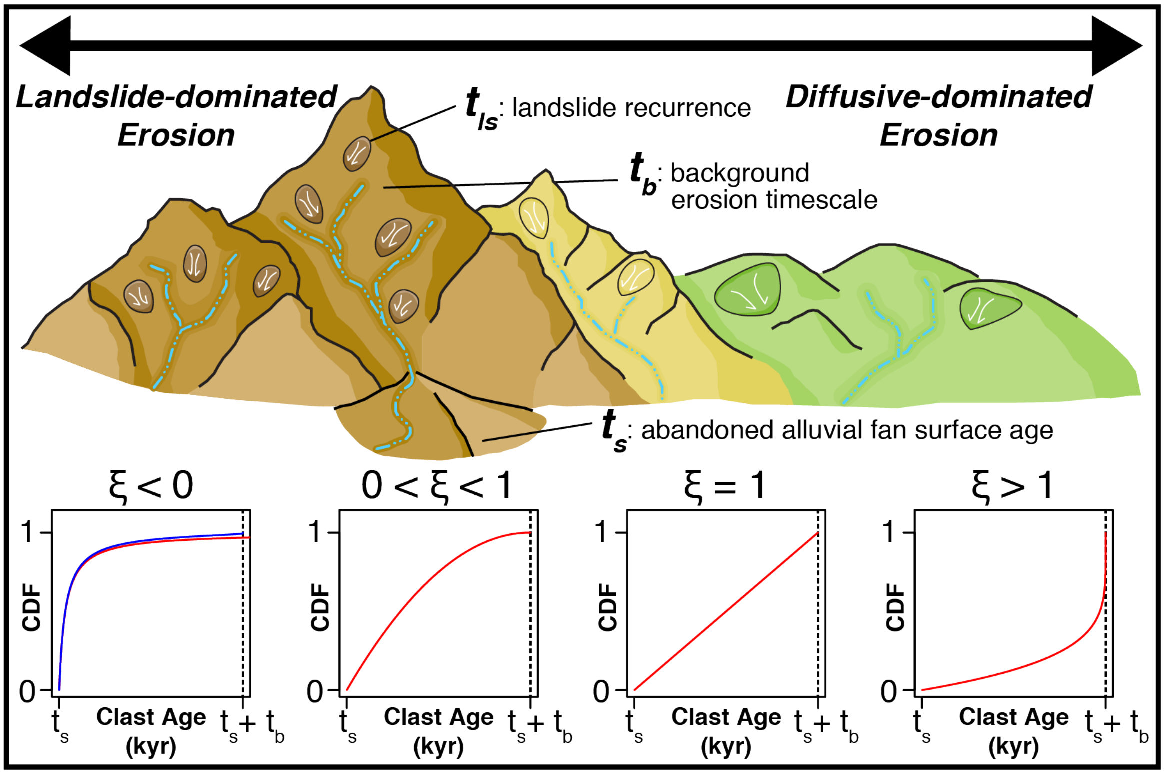

Fig. 1. Schematic catchment model of landslide erosion's influence on clast-age distribution. Red lines show clast-age distributions modeled as generalized Pareto cumulative distribution functions (CDFs). Decreasing values of the shape parameter, $\boldsymbol{\xi}$, are indicative of catchments where erosion by landslides contributes proportionally more sediment to drainages than erosion by soil formation and diffusive down-slope transport. For positive values, $\boldsymbol{\xi}$ may be interpreted as $\boldsymbol{t_{ls}/t_b}$, the ratio of average landslide recurrence, derived with a Poisson landslide recurrence model, to background erosion timescale, defined as the time required to erode through one e-folding length scale (~60 cm in rock; Lal, 1991). Negative $\boldsymbol{\xi}$ values require long-tailed, non-

Poisson landslide recurrence. Blue line shows an equivalent CDF derived with Pareto-distributed (long-tailed) landslide return times (see Section 2.1).

2. Model Derivation and Distribution-fitting Approach

2.1 Clast-age model derivation

Following the approach of previous studies (Niemi et al., 2005; Yanites et al., 2009), we model catchment erosion as a combination of landslides, which episodically erode and reset the nuclide concentration in catchment walls, and diffusive background erosion processes, which steadily erode the surface between landslide events. Our analytical approach does not directly account for the volume of landslides. Rather, we derive the TCN concentration in clasts eroded from the catchment wall following the most recent landslide event. This has been shown to compare well with numerical simulations that explicitly account for landslide volume (e.g., Yanites et al., 2009).

Between landslide events, the catchment wall undergoes a steady, background regolith erosion rate, E_b, during which TCNs accumulate according to an exponential ingrowth curve approaching a maximum steady-state effective exposure age, $t_b = z^*/E_b$, where $z*$ is the e-folding length of TCN production by nuclide spallation (~60 cm for a typical bedrock density of 2.7 g/cm^3, Fig. 1)(e.g., Lal, 1991). We refer to t_b herein as the background erosion timescale. Background erosion is an aggregate term that refers to any diffusive erosional process, such as soil creep. Starting with zero TCN concentration, the effective TCN age of the catchment wall, and thus the effective age of sediment clasts derived from that portion of the landscape (t_c), exponentially approaches t_b:

$$t_c = t_b\left(1 - e^{-t/t_b}\right) \tag{1}$$

In accordance with previous studies (Niemi et al., 2005; Yanites et al., 2009), we initially choose to model landslide recurrence as a Poisson process with a wait time probability distribution function (PDF):

$$PDF(wt) = \frac{1}{t_{ls}} e^{-t/t_{ls}} \quad (2)$$

where t_{ls} is the mean wait time between landslides at every point within a catchment. A Poisson model implies that wait times between landslides are spatiotemporally uncorrelated (e.g., Crovelli, 2000; Witt et al., 2010; Yanites et al., 2009).

Combining landslide recurrence and TCN ingrowth yields a probabilistic model for the past exposure history of a landscape from which a sediment sample is derived. We determine the probability distribution function (PDF) of clast ages due to TCN ingrowth and landslide renewal by substituting the relation for background erosion (t_c, Eq. 1) into the Poisson PDF of landslide recurrence and multiply by the Jacobian derivative (dt/dt_c) to maintain probability (Yanites et al., 2009):

$$PDF(t_c) = PDF\big(wt, t = f(t_c)\big) dt/dt_c \quad (3)$$

where $t = -t_b \ln{(1 - t_c/t_b)}$ and $\frac{dt}{dt_c} = \frac{1}{1-\frac{t_c}{t_b}}$. The result is a generalized Pareto distribution (GPD) of clast ages, t_c:

$$PDF(t_c) = \frac{1}{t_{ls}} \left[1 - \frac{t_c}{t_b}\right]^{t_b/t_{ls} - 1} \quad (4)$$

The cumulative distribution function (CDF) associated with this PDF is found by integrating Eq. 4 from 0 to t_c, and allowing for a shift, t_s, due to post-depositional aging of the deposit (the target surface age of datasets used in this study):

$$CDF_{GPD}(t_c) = 1 - \left[1 - \frac{(t_c - t_s)}{t_b}\right]^{t_b/t_{ls}} \quad (5)$$

This CDF is the three-parameter form of the GPD. The three parameters of the GPD are known as location, shape, and scale, which taken together describe its general form. Location defines the intercept of a dataset's GPD distribution (where $CDF_{GPD} = 0$), shape defines its concavity, and scale defines its curvature. Under the conditions of Poisson landslide recurrence, t_s, $\xi = {t_{ls}}/{t_b}$, and $\sigma = t_{ls}$ are the location, shape, and scale parameters of the GPD distribution, respectively. These parameters reveal the post-depositional age of the surface from which the sample was collected (t_s), and two timescales related to erosion of the source catchment: average landslide recurrence (t_{ls}), and background erosion timescale (t_b).

Long-tailed GPD distributions of clast ages, described by $\xi < 0$, cannot be explained by Poissonion landslide recurrence, because neither t_b nor t_{ls} may be negative. Instead, the underlying landslide wait time model must also be a long-tailed. To explore this, we recast our derivation using a member of the Pareto distribution family, the Lomax distribution (Lomax, 1954), for the landslide wait time:

$$PDF_{LO}(wt) = \frac{\alpha}{\beta}\left[1 + \frac{t}{\beta}\right]^{-(\alpha+1)} \quad (6)$$

The parameters α and β are the tail and scale parameters, respectively, of this distribution. The mean landslide return time is $\beta/(\alpha - 1)$. Note that these parameters are distinct from the shape and scale parameters defined by eq. 5, though they are related, as shown below.

The derivation for $PDF_{LO}(t_c)$ follows the same steps as above for the Poisson case (eqs. 1-5). For clarity, we omit shifting the distribution by a location value, t_s. The resulting PDF and CDF are:

$$PDF_{LO}(t_c) = \frac{\alpha}{\beta}\left[1 - \frac{t_b}{\beta}\ln\left(1 - \frac{t_c}{t_b}\right)\right]^{-(\alpha+1)} \frac{-t_b}{1 - \frac{t_c}{t_b}} \tag{7}$$

$$CDF_{LO}(t_c) = 1 - \left[1 - \frac{t_b}{\beta}\ln\left(1 - \frac{t_c}{t_b}\right)\right]^{-\alpha} \tag{8}$$

$CDF_{LO}(t_c)$ is closely related to eq. 5. In the limit where $t_b \gg 0$, the natural logarithm term may be approximated with the first term of its Taylor series:

$$\ln\left[1 - \frac{t_c}{t_b}\right] \approx -\frac{t_c}{t_b} \tag{9}$$

Substitution into $CDF_{LO}(t_c)$ yields:

$$CDF_{LO}(t_c) \approx 1 - \left[1 + \frac{t_c}{\beta}\right]^{-\alpha} \tag{10}$$

This CDF is a GPD, analogous to eq. 5, but with $\xi = -{}^{1}/_{\alpha}$ as its shape, and $\sigma = {}^{\beta}/_{\alpha}$ as its scale parameter. Therefore, as background erosion rate approaches zero ($t_b \gg 0$), the distribution of clast ages reflects the distribution of landslide recurrence (eq. 6).

Depending on the ratio t_b/β in eq. 8, it may be difficult to discriminate Poisson- and Pareto-distributed landslide recurrence with limited dataset sizes and TCN measurement uncertainty (Fig. 2). Fortunately, prediction of the location parameter, t_s, is insensitive to the choice of landslide wait-time distribution. However, there are trade-offs between the other distribution parameters that do depend on this choice. We rely on the GPD clast-age distribution (eq. 5) to model available datasets, including approximation of long-tailed cases, and defer application of the full Pareto-distributed landslide model (eq. 8) for future study, as fitting this model requires larger exposure-age data sets than are currently available.

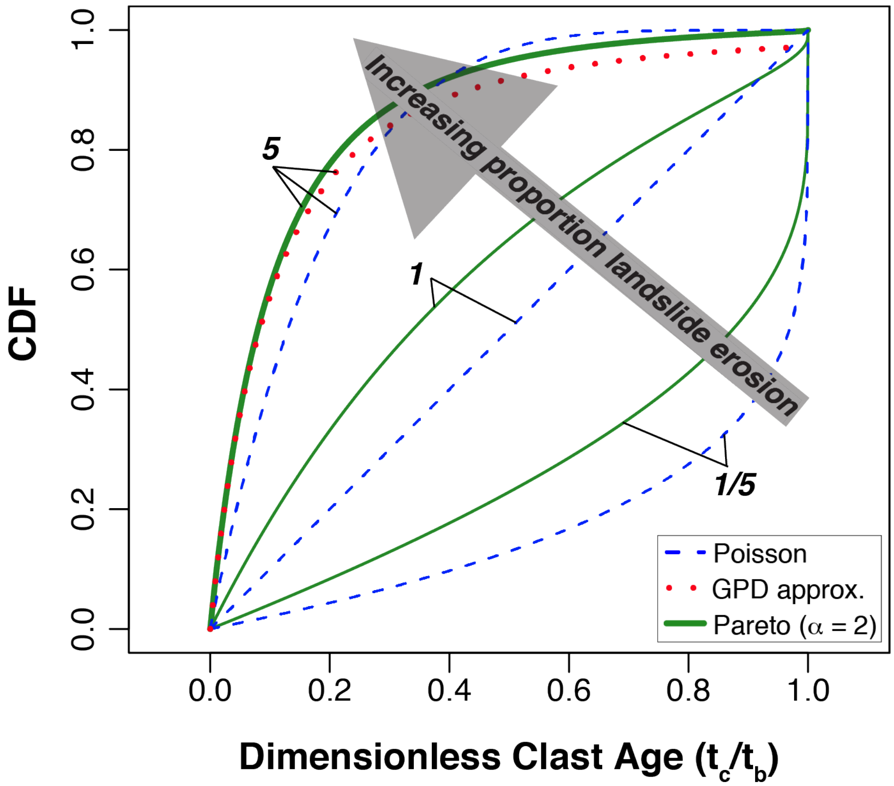

Fig. 2. Predicted cumulative distribution functions of clast ages derived with Poisson (blue dashes) and Pareto (thick, solid green) models of landslide wait time. Clast ages are normalized by background erosion time scale, t_b. Labels indicate mean landslide return time, t_{ls}, normalized by t_b for each curve (ξ for Poisson-derived distributions, $\beta/t_b(\alpha-1)$ for Pareto-derived distributions). These distributions are similar in form when $t_{ls} \gg t_b$. Dotted red line shows GPD approximation for $\alpha = 2$ ($\xi = -1/2$) case with $t_{ls}/t_b = 5$. This approximation diverges from the analogous Pareto-derived clast-age model in the distribution tail, at CDF > 0.75.

Several processes that affect TCN concentration in sediments are not included in our models. We neglect TCN radioactive decay, an appropriate assumption given the long half-life of ^{10}Be (1.3 Myr) with respect to erosion rates and sediment residence times in the landscape (e.g., Granger, 2006; Lal, 1991). We also neglect TCN concentrations acquired during transport following erosion from the catchment walls and prior to deposition within an alluvial fan or stream terrace, nor do we account for complicated burial histories or reworking of clasts from upstream deposits. These assumptions are appropriate for short transport distances and catchments with little sediment storage (Yanites et al., 2009), consistent with the settings of clast-age datasets we analyze. We assume that the surface TCN concentration will be reset after each landslide. However, this assumption is not valid for small (<100 m^2) shallow landslides that excavate only partway through the upper ~2 m (the approximate depth for 95% of TCN production by spallation)(Lal, 1991). Effectively, the smallest landslides contribute to background erosion, rather than resetting the TCN concentration of their footprint.

2.2 Fitting the model to clast-age distributions

We apply a Bayesian Markov chain Monte Carlo (MCMC) algorithm to sample the posterior distributions of the three parameters of our GPD model for each data set (Fig. 3). In multivariate analyses, MCMC algorithms are used to determine the summary statistics of sample populations where analytical solutions are hampered by model complexity (e.g. Andrieu et al., 2003). We fit the cumulative GPD to clast ages arranged in rank order, which implicitly assumes that the underlying distribution was sampled sufficiently and uniformly.

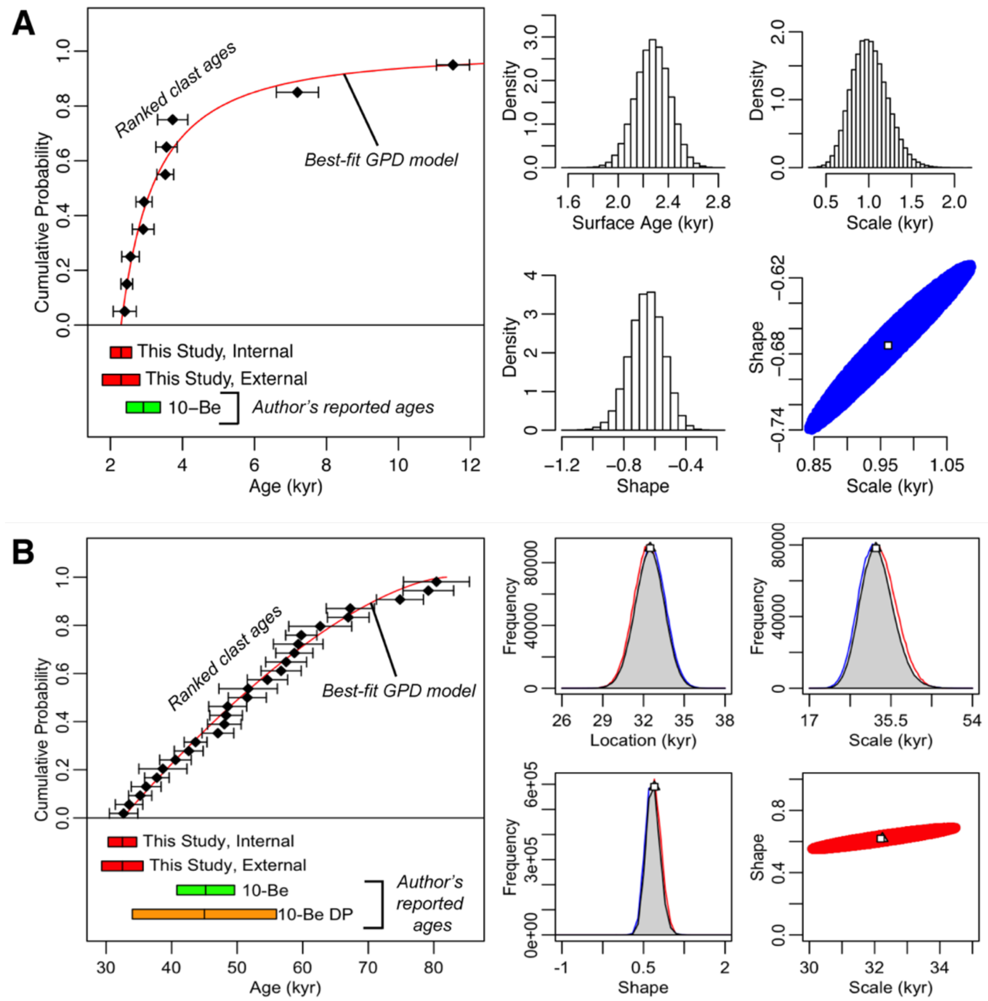

Fig. 3. Annotated example outputs of MCMC algorithm to determine best-fit GPD model to clast age datasets. A) output for ξ-parameterized algorithm, B) output for combination of θ and ξ parameterizations. Diamonds and error bars (two standard deviations, analytical uncertainty only) indicate individual ranked clast ages. Best-fit GPD model indicated by red line. Below x-axis are output ages determined in this study (red bars, 95% range of best-fit solutions) including ages calculated using analytical error only, as well as external error due to TCN production rate uncertainty. If reported, ages determined by publishing authors using ^{10}Be clasts and other geochronometers are included. DP = depth profile. Right side of each figure shows histograms of accepted output parameters of location (t_s), scale (σ), and shape (ξ). Covariance of σ and

ξ indicated by bottom right figure, showing best-fit (white box) and field (red or blue) of best 5% of MCMC-derived parameter fits. Red and blue lines in B indicate results of ξ and θ algorithms (see text); gray fields are merged probability distributions for each model parameter.

We determine an initial fit of ξ and σ using the method of moments (Hosking and Wallis, 1987) and a linear combination of order statistics to determine the best-fit t_s value (Sazlvadori, 2002). For each parameter, we set the search space (the Bayesian initial prior distribution) to be a wide normal distribution centered on the initial fit. The step size sample space for each iteration of the MCMC algorithm is also a normal distribution with a standard deviation that is 5% of the standard deviation for the initial prior for each parameter. Culling of parameter values is achieved using log-likelihood minimization with a rejection criterion to eliminate poor distribution fits. Standard deviation values for the initial prior distribution and step size are varied together to achieve a 20 to 30% acceptance range, which we consider a satisfactory search of the available parameter space. We improve on these initial GPD fits over 2 million realizations of our MCMC algorithm. Acceptable parameter values for the GPD tend to be normally distributed about the best-fit values (Fig. 3).

The range of the shape parameter, ξ , of the GPD distribution includes two limiting cases. When $\xi = 0$, the GPD simplifies to an exponential distribution, and when $\xi = 1$ the GPD behaves as a uniform distribution (e.g., de Zea Bermudez and Kotz, 2010; Hosking and Wallis, 1987). Our algorithm is largely capable of sampling around the limiting case of $\xi = 0$ without attrition in the search space of ξ . However, as ξ approaches and exceeds 1, the change in behavior of the GPD (as evidenced by a flip in its concavity, Figs. 1 and 2) requires a different algorithmic approach. This behavior has been noted previously (de Zea Bermudez and Kotz, 2010). In order to sample values of shape near 1 ($t_{ls} \approx t_b$ for Poisson landslide recurrence), we introduce an alternative parameterization of the GPD by the exponent $\theta = \sigma/\xi$:

$$CDF_{GPD}(t_c) = 1 - \left[1 - \frac{(t_c - t_s)}{\theta}\right]^{\theta/\sigma}. \quad (11)$$

In this parameterization, we restrict the search range of θ to 0 – 650 kyr.

The best-fit GPD for most datasets can be determined using one of these two representations. However, for datasets with a ξ between 0.5 and 1.5, the search spaces and resulting best-fit distribution of shape values are truncated near the limiting value of 1. In these cases, the MCMC outputs from the θ and ξ parameterizations are combined to represent the summary statistics of the best-fit GPD (Fig. 3b). Distributions for all three GPD parameters are determined using both algorithms and merged using a linearly tapered weighting scheme for shape values between 0 and 1. The corresponding t_s and t_{ls} parameters are also weighted according to this scheme. Summary statistics and best-fits of the combined model runs are then recalculated from the resulting histograms of the model parameters.

3. Application of clast-age model

3.1 Synthetic tests

Given the small sample sizes of most available published datasets, the distribution of clast ages may not be adequately sampled to correctly model the GPD. In order to determine a viable sample size for fitting the GPD to clast-age distributions, we used our MCMC algorithm to fit the GPD to synthetically generated GPD datasets (Fig. 4). We sampled from two known distributions where $\xi = -0.5$ (upper row, Fig. 4) and $\xi = 0.75$ (lower row, Fig. 4). For the known distribution with a negative-valued ξ, we set $t_s = 5$ ka. For the positive-valued ξ dataset, $t_s = 25$ ka. For both datasets, we set $\sigma = 10$ ka. For both known distributions, we generated random samples ranging from 5 to 50 individual measurements (equivalent to 5 or 50 cobble or boulder measurements). For each possible dataset size, we generated 100 random realizations and produced a model result for each.

Our synthetic tests show that the GPD CDF should ideally be fit to 14 or more samples. Estimates for surface age (t_s) and shape (ξ) converge more readily than distribution scale (σ). At sample sizes greater than 14, decreased uncertainty in GPD parameters is offset by production rate uncertainty, which we take to be ~10-20% (e.g., Borchers et al., 2016; Lifton et al., 2014; Marrero et al., 2016; Phillips et al., 2016). Because few published datasets with 14 or more individual clast measurements exist globally (*n* = *6*), we set a lower threshold of 8 individual clast measurements to balance adequate representation of the GPD while casting more widely across the published literature *(n = 64)*.

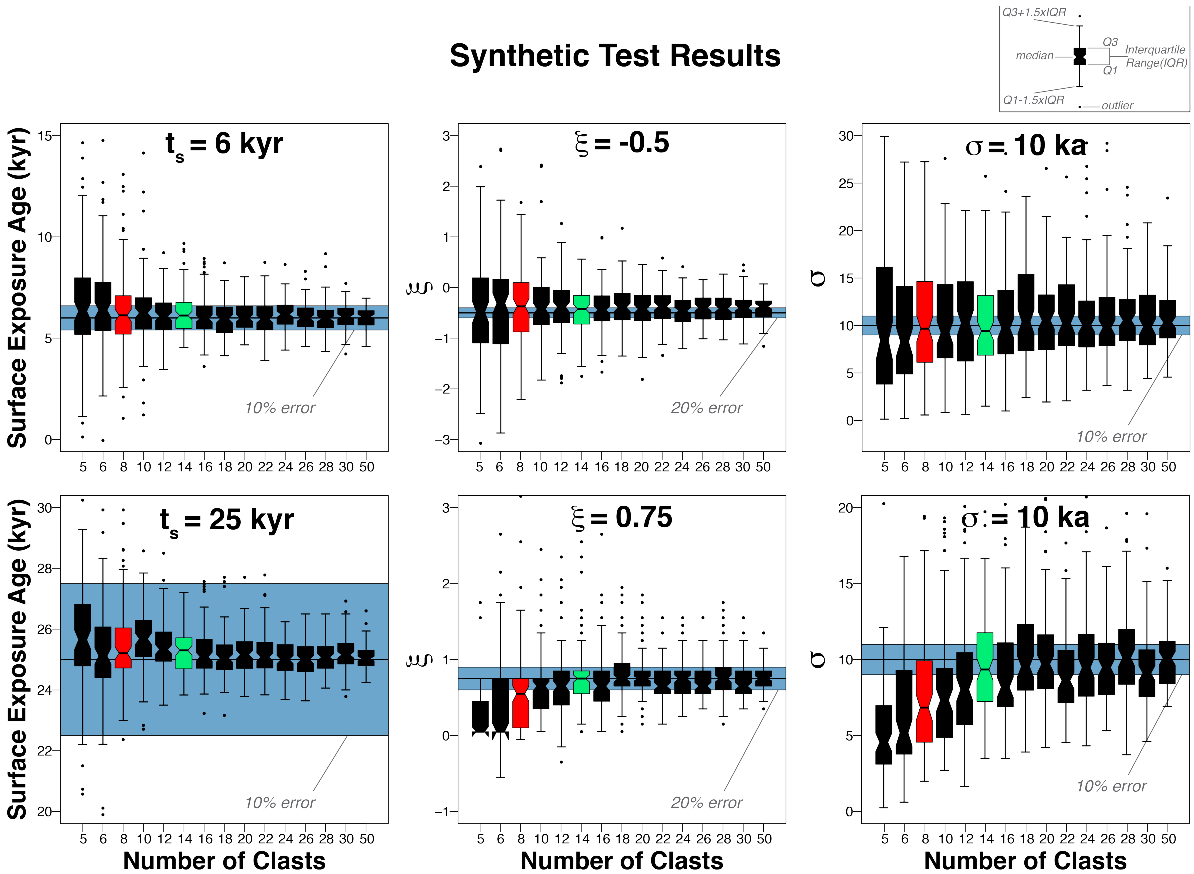

Fig. 4. Whisker plot results of synthetic tests fitting the GPD model to randomly sampled, known distributions, arranged by increasing sample number. Note that horizontal axis scale is nonlinear. Boxes show the interquartile range for 100 synthetic tests of varying dataset sizes. Explanatory whisker plot output shown at upper right. Blue bands show 10% (t_s, σ) or 20% (ξ) acceptable range for fit distribution parameters. Synthetic tests illustrate the effect of low sample size on model outputs for two representative cases: upper row, $\xi = -0.5$; lower row: $\xi = 0.75$. Although *n* = 8 (red whisker plot) datasets have a higher spread in output parameter values than larger synthetically tested dataset sizes, it is sufficient improvement over *n* = 5 to justify culling smaller sample sizes. These tests suggest that future studies should strive for datasets of at least *n* = 14 (green whisker plot) to adequately characterize the GPD.

3.2 Application to published data sets

To demonstrate the applicability of the GPD clast-age model, we estimate the best-fit CDF for 64 clast-age distributions from ^{10}Be datasets drawn from the literature (Fig. 5, Tables S1 and S2, Data S1). All were collected to date stream terraces and alluvial fans, with the majority displaced by active faults (Table S1). We use the authors' calculated exposure ages at the sample site and neglect the impact of increasing production rate with catchment elevation (Lal, 1991). This is valid for determining target surface age, and should not affect estimates of $\boldsymbol{\xi}$ unless landslide frequency and background erosion rate vary with elevation or if the grains sampled are dominantly produced in limited parts of the landscape (Lukens et al., 2016; Riebe et al., 2015).

We filter the global datasets to ensure that each dataset represents a single catchment source, consists only of single clasts, and includes ≥8 measurements. The majority of data meeting these criteria come from either southwest North America (n = 20) or Asia (n = 38), where exposure age-dating has been widely applied to fault slip-rate studies. Six additional datasets are found in Peru (n = 3) and along the Dead Sea fault zone (n = 3). A summary table of final GPD outputs determined using the MCMC algorithm is presented in Table S2. Over 45% of our GPD model fits (29/64) result in negative $\boldsymbol{\xi}$ values, with the majority of these collected in interior Asia (Fig. 5).

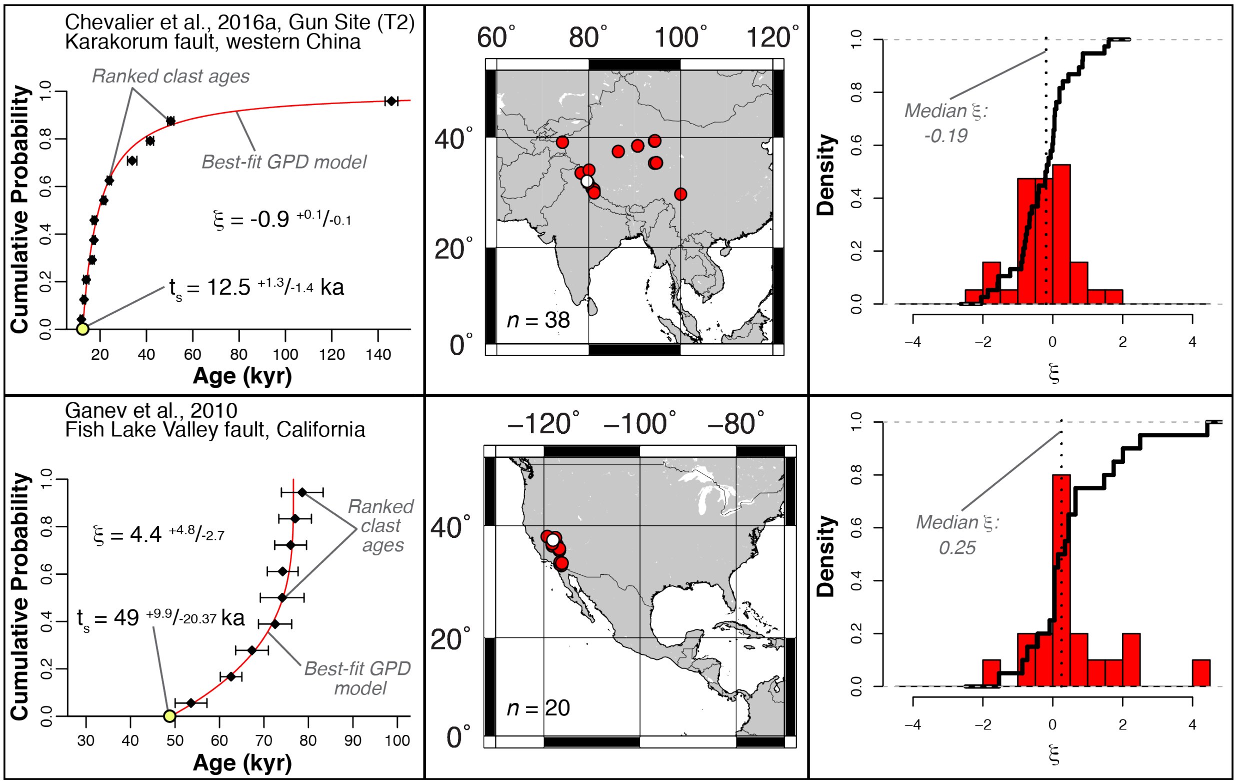

Fig. 5. Comparison of typical datasets from the American southwest and Asia. Datasets from the American southwest are more often characterized by $\boldsymbol{\xi} \geq \mathbf{0}$ (lower panel, Ganev et al., 2010). Datasets from Asia tend towards $\boldsymbol{\xi} < \mathbf{0}$ (upper panel, Chevalier et al., 2016). Red points show geographic distribution of datasets in these regions. White points indicate locations of example datasets at left. Right column shows histograms and empirical CDFs of observed $\boldsymbol{\xi}$ values in Asia (upper panel) and the American southwest (lower panel).

3.3 Identification and removal of young outliers in clast-age distributions

All outliers identified by the publishing authors are included in our models, with the exception of seven datasets where young outliers cause a statistically significant shift in the ξ parameter of the best-fit distribution. We interpret these outliers as clasts that either toppled or were exhumed by erosion of the sampled deposit. We identified by visual inspection ten datasets from seven publications that contain possible young outliers (Fig. 6, Table S3). To objectively identify these outliers, we remove samples from datasets based on the statistical significance of the change to the σ and ξ parameters they impose on the resultant best-fit GPD distribution. For all datasets suspected of containing young outliers, we calculate two best-fit GPD distributions: one that includes the suspected outlier sample, and one where the outliers are removed. If more than one young outlier is suspected, we calculate as many additional GPD distributions as there are suspected outliers (Table S3). If the best-fit shape parameter calculated for the dataset following outlier removal deviates from the 95% confidence range of the ξ parameter calculated when the suspected outlier is included, then the outlier is removed (Fig. 6, Fig. S1). We take this conservative approach to outlier removal in order to restrict the amount of subjective culling of samples from these datasets. Of the ten datasets that were flagged for containing potential young outliers, seven were confirmed to include outliers according to our criteria (Table S3).

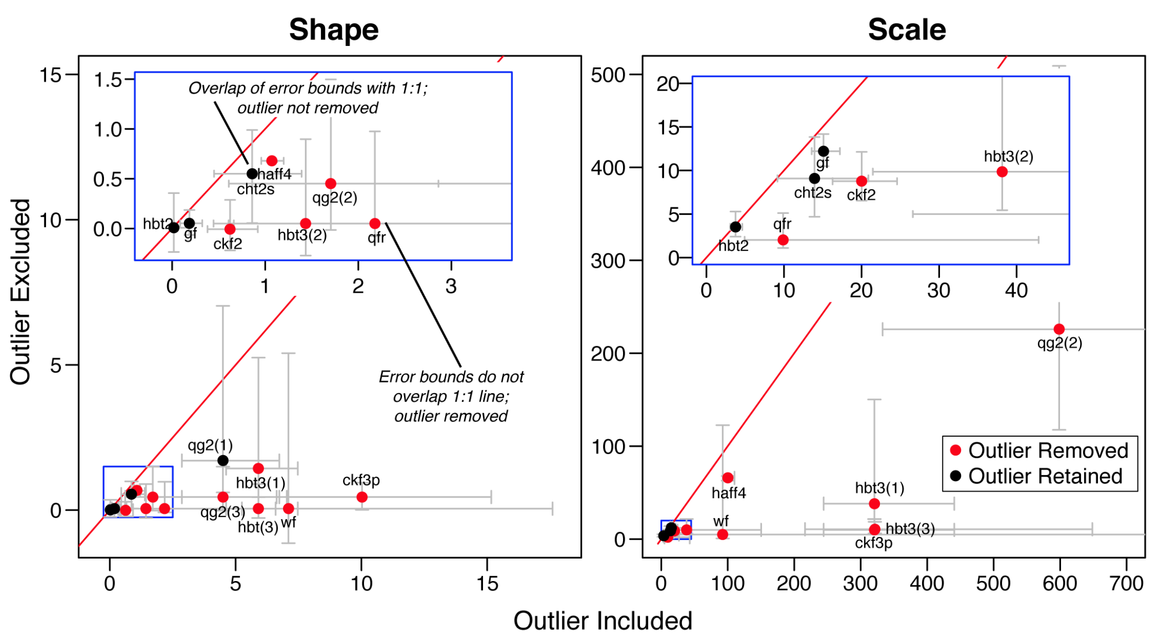

Fig. 6. Methodology of outlier removal for selected datasets. Axes indicate best-fits and 95% error bounds to shape (ξ) and scale (σ) parameters for datasets where outlier is included (vertical

axis) and where outlier is excluded (horizontal axis). Units of ξ are dimensionless. Units of σ are in kyr. Blue boxes in both figures indicate inset region. Outliers are removed if error bounds do not cross 1:1 line (red), indicating a statistically significant change in fit of parameters due to outlier removal. See Table S3 for label key and parameter outputs for each dataset and removal decision. The σ fit to the Qg2 surface (Dühnforth et al., 2017) with no outliers removed plots well outside of shown range; comparisons of removal of two outliers are therefore not included but are given in Table S3. Only one dataset recorded a statistically significant change in ξ that was not accompanied by a significant change in σ (wf; Zehfuss et al., 2001); we removed the outlier from this dataset as well.

4. Discussion

An immediate and widely applicable result of our GPD clast-age model is a rigorous estimate of the exposure age of a target surface. Using our algorithm, the best-fit $\boldsymbol{t_s}$ value of the GPD is the target deposit age, with uncertainty derived from the MCMC analysis (Fig. 3). The GPD model yields younger surface ages than reported by the publishing authors (Fig. 7a). Importantly, when $\boldsymbol{\xi < 1}$, the clustering of the youngest samples defines a rank-age slope of the GPD, and therefore estimates of $\boldsymbol{t_s}$ are not overly sensitive to sampling the youngest available surface clast (Fig. 3).

To validate age estimations from the GPD model, we compare our results with independent geochronometers used by publishing authors at ten sites (Fig. 7b), including TCN depth-profiles (Anderson et al., 1996). We find that $\boldsymbol{t_s}$ agrees with these independent ages, with the exception of four sites with older Carbon-14 dates from materials collected within the underlying deposits, as should be expected, and two sites where the fitted location parameter clearly underestimates U-series ages from soil carbonates and a ^{10}Be depth profile. In these cases, erosion of the target surfaces has led to exhumation of clasts from the alluvial fan deposits, with incomplete exposure over the lifetime of the fan surfaces (Behr et al., 2010; Blisniuk et al., 2013). Our inheritance model does not account for the effects of post-depositional modification of target surfaces. Generally, erosion is less of a concern for clasts that are too large to be transported across stable fan surfaces, unless erosion of surrounding materials has been sufficient to exhume clasts from depth (e.g. Behr et al., 2010). Most of the sites we examine are young deposits (<50 ka) and unlikely to have eroded sufficiently to expose younger clasts.

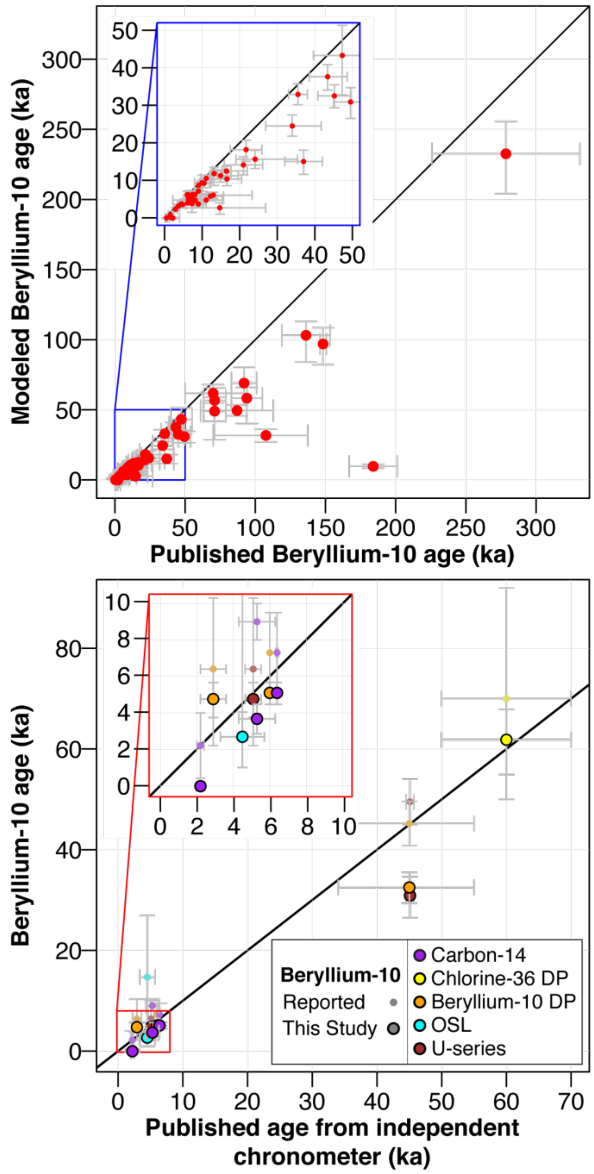

Fig. 7. ^{10}Be age adjustments and comparison with additional geochronometers. Top: Comparison between published and modeled ages determined from ^{10}Be surface clast datasets. Note systematically younger modeled ages. Bottom: Comparison of published and modeled ages with independent geochronometers, including TCN depth profiles, as reported by publishing authors. In most cases our modeled ages lie closer to the independent ages, indicated by the 1:1 line. Annotated version of lower figure included in extended data (Fig. S1).

Negative ξ values occur frequently in the arid interior of Asia and a subset of the most arid regions of the southwestern United States. These populations are characterized by strongly curved, concave-down cumulative age distributions (Fig. 1), with the oldest clasts several tens of thousands of years older than the youngest. The commonality of these long-tailed distributions argues against contamination by recycled sediments as a rationale for removal of older ages as outliers. We hypothesize that long-tailed populations of clast ages appear in these settings because of negligible background erosion, such that the underlying distribution of landslide wait times largely controls the exposure of bedrock. Long-tailed (e.g. Pareto-distributed) landslide recurrence behavior likely occurs in more humid settings as well, but is obscured by higher rates of background erosion. With infrequent landslides, clast-age distributions derived with Pareto-distributed landslide recurrence (eq. 8) become indistinguishable from the results of a Poisson-based recurrence model (Fig. 2).

A long-tailed distribution of landslide recurrence implies that recent landslide sites are more likely to be reactivated than areas of longer-term stability. This results in spatial and temporal clustering of landslide triggering, alternating with time-dependent stabilization of the landscape. To date, few datasets exist to corroborate such a temporal distribution of landslides at the catchment scale. A power-law distribution of landslide wait times has been suggested for a 50-year record of landslide activity in Italy (Rossi et al., 2010). Power spectral analyses of this same dataset confirms temporal clustering (Witt et al., 2010). Temporal clustering of landsliding may be driven by the underlying distribution of triggering events, such as rainfall or earthquakes (e.g., McPhillips et al., 2014; West et al., 2014). Spatial variation of landslide recurrence time may correspond to the observed variation of catchment hillslope curvature, from creepdominated, strongly curved ridge crests to steep, planar landslide-dominated slopes (e.g., Hurst et al., 2012; Roering et al., 1999).

By fitting the full range of clast ages, our modeling approach yields mean inherited exposure age, $\overline{\boldsymbol{t_c}}$, and thus catchment mean erosion rate, $\boldsymbol{E} = \boldsymbol{z}^*/\overline{\boldsymbol{t_c}}$, from the parameters of the GPD distribution. This complements the widely applied technique of measuring $\overline{\boldsymbol{t_c}}$ from well-mixed sand samples (Granger, 2006). The mean value of the GPD, $\overline{\boldsymbol{t_c}} = \boldsymbol{\sigma}/(\mathbf{1}+\boldsymbol{\xi})$, exists for $\boldsymbol{\xi} > -\mathbf{1}$. A mean value also exists for clast ages predicted from Pareto-distributed landslide recurrence, even for heavy-tailed cases $(\boldsymbol{\xi} \leq -\mathbf{1})$, because the distribution truncates at $\boldsymbol{t_b}$ (Fig. 1).

Our mechanistic model for the distribution of clast exposure ages provides a rationale for removing inheritance from landform ages and a framework for assessing landslide recurrence behavior and erosion rate from the distribution parameters. By revealing the balance of physical erosion mechanisms, clast populations can provide essential information for understanding chemical cycling through the critical zone. Because the distribution of clast ages is insensitive to post-depositional exposure history, this tool may be applied to ancient deposits as well as modern river sediments. The frequent occurrence of long-tailed clast-age populations suggests that landslide wait times are Pareto-distributed, and thus temporally or spatially clustered, with important implications for quantifying landslide hazard. Reduction in surface age of all datasets examined in this study necessitates a reevaluation of fault slip rates at the original study sites, which will influence models of earthquake hazard.

4. Conclusions

We present a mechanistic model of inheritance recorded in surface clast datasets that encompasses the effects of episodic landsliding and steady background erosion on recorded TCN concentration. We propose that a generalized Pareto distribution characterized by three parameters – post-depositional surface age (t_s), shape (ξ), and scale (σ) – should be used to fit clast-age distributions. For the case of Poisson landslide recurrence, the scale parameter corresponds to mean landslide recurrence time and the shape parameter is the ratio of background erosion timescale to this recurrence time. To apply the GPD distribution, we developed a Monte Carlo Markov Chain algorithm to fit this model to surface clast datasets. By fitting the GPD to 64 Beryllium-10 datasets drawn from a global literature survey, we show that this model can be applied to clast-age distributions sourced from a variety of geographic settings.

The abundance of datasets with negative ξ indicates that a Poisson model of landslide return time is inadequate. We propose a Pareto landslide wait time model to explain these datasets, and show that this model may be approximated by the GPD where background erosion rates are low. In other settings, it is difficult to discriminate Poisson- and Pareto-based landslide recurrence, given the small sample sizes of current Beryllium-10 datasets.

Application of our GPD model results in younger surface ages than previously published. We show that in most cases, our new age determinations better correspond to ages from independent Quaternary geochronometers. In addition to improved exposure age dating, the distribution of clast ages reveals the balance of erosion processes operating across the landscape. This opens the door to new applications of TCN geochronology to quantify erosion in upstream catchments.

Acknowledgments

The authors thank Lewis Owen and Jing Liu-Zeng for numerous discussions that helped in the development of this project. We thank Magali Billen, Maxwell Rudolph, Isabel Montañez, Sujoy Mukhopadhyay, and Don Turcotte for early reviews of the manuscript. This effort was supported by National Science Foundation [award number EAR-1524734] and the Southern California Earthquake Center [grants #15209 and #17121].

Both authors contributed equally to the preparation of this manuscript. The authors declare no competing interests.

References

Anderson, R.S., Repka, J.L., Dick, G.S., 1996. Explicit treatment of inheritance in dating depositional surfaces using in situ 10Be and 26Al. Geology 24, 47–51. https://doi.org/10.1130/0091-7613(1996)024<0047:ETOIID>2.3.CO

Andrieu, C., De Freitas, N., Doucet, A., Jordan, M.I., 2003. An introduction to MCMC for machine learning. Mach. Learn. 50, 5–43. https://doi.org/10.1023/A:1020281327116

Behr, W.M., Rood, D.H., Fletcher, K.E., Guzman, N., Finkel, R., Hanks, T.C., Hudnut, K.W., Kendrick, K.J., Platt, J.P., Sharp, W.D., Weldon, R.J., Yule, J.D., 2010. Uncertainties in slip-rate estimates for the Mission Creek strand of the southern San Andreas fault at Biskra Palms Oasis, southern California. Bull. Geol. Soc. Am. 122, 1360–1377. https://doi.org/10.1130/B30020.1

Blisniuk, K., Oskin, M., Mériaux, A.S., Rockwell, T., Finkel, R.C., Ryerson, F.J., 2013. Stable, rapid rate of slip since inception of the San Jacinto fault, California. Geophys. Res. Lett. 40, 4209–4213. https://doi.org/10.1002/grl.50819

Borchers, B., Marrero, S., Balco, G., Caffee, M., Goehring, B., Lifton, N., Nishiizumi, K., Phillips, F., Schaefer, J., Stone, J., 2016. Geological calibration of spallation production rates in the CRONUS-Earth project. Quat. Geochronol. 31, 188–198. https://doi.org/10.1016/j.quageo.2015.01.009

Brown, E.T., Stallard, R.F., Larsen, M.C., Raisbeck, G.M., Yiou, F., 1995. Denudation rates determined from the accumulation of in situ-produced 10Be in the luquillo experimental forest, Puerto Rico. Earth Planet. Sci. Lett. 129, 193–202. https://doi.org/10.1016/0012-821X(94)00249-X

Cerling, T.E., Craig, H., 1994. Geomorphology and In-Situ Cosmogenic Isotopes. Annu. Rev. Earth Planet. Sci. 22, 273–317.

Chevalier, M.L., Der Woerd, J. Van, Tapponnier, P., Li, H., Ryerson, F.J., Finkel, R.C., 2016. Late Quaternary slip-rate along the central Bangong-Chaxikang segment of the Karakorum fault, western Tibet. Bull. Geol. Soc. Am. 128, 284–314. https://doi.org/10.1130/B31269

Crovelli, R.A., 2000. Probability models for estimation of number and costs of landslides, US Geological Survey Open-File Report 00-249.

Dadson, S.J., Hovius, N., Chen, H., Dade, W.B., Hsieh, M.-L., Willett, S.D., Hu, J.-C., Horng, M.-J., Chen, M.-C., Stark, C.P., Lague, D., Lin, J.-C., 2003. Links between erosion, runoff variability and seismicity in the Taiwan orogen. Nature 426, 648–651.

de Zea Bermudez, P., Kotz, S., 2010. Parameter estimation of the generalized Pareto distribution-Part I. J. Stat. Plan. Inference 140, 1353–1373. https://doi.org/10.1016/j.jspi.2008.11.020

Dühnforth, M., Densmore, A.L., Ivy-Ochs, S., Allen, P., Kubik, P.W., 2017. Early to Late Pleistocene history of debris-flow fan evolution in western Death Valley (California) using cosmogenic 10Be and 26Al. Geomorphology 281, 53–65. https://doi.org/10.1016/j.geomorph.2016.12.020

Emberson, R., Hovius, N., Galy, A., Marc, O., 2016. Chemical weathering in active mountain belts controlled by stochastic bedrock landsliding. Nat. Geosci. 9, 42–45. https://doi.org/10.1038/ngeo2600

Gabet, E.J., 2007. A theoretical model coupling chemical weathering and physical erosion in landslide-dominated landscapes. Earth Planet. Sci. Lett. 264, 259–265. https://doi.org/10.1016/j.epsl.2007.09.028

Ganev, P.N., Dolan, J.F., Frankel, K.L., Finkel, R.C., 2010. Rates of extension along the Fish Lake Valley fault and transtensional deformation in the Eastern California shear zone-Walker Lane belt. Lithosphere 2, 33–49. https://doi.org/10.1130/L51.1

Gosse, J.C., Phillips, F.M., 2001. Terrestrial in situ cosmogenic nuclides: theory and application. Quat. Sci. Rev. 20, 1475–1560.

Granger, D.E., 2006. A review of burial dating methods using 26 Al and 10 Be A review of burial dating methods using 26 Al and 10 Be. Geol. Soc. Am. Spec. Pap. 415, 1–16. https://doi.org/10.1130/2006.2415(01).

Granger, D.E., Riebe, C.S., 2013. Cosmogenic Nuclides in Weathering and Erosion, 2nd ed, Treatise on Geochemistry: Second Edition. Elsevier Ltd. https://doi.org/10.1016/B978-0-08-095975-7.00514-3

Hosking, J.R.M., Wallis, J.R., 1987. Parameter and quantile estimation for the generalized Pareto distribution. Technometrics 29, 339–349. https://doi.org/10.2307/1269343

Hurst, M.D., Mudd, S.M., Walcott, R., Attal, M., Yoo, K., 2012. Using hilltop curvature to derive the spatial distribution of erosion rates. J. Geophys. Res. 117, F02017.

https://doi.org/10.1029/2011JF002057

Korup, O., Densmore, A.L., Schlunegger, F., 2010. The role of landslides in mountain range evolution. Geomorphology 120, 77–90. https://doi.org/10.1016/j.geomorph.2009.09.017

Kump, L.R., Brantley, S.L., Arthur, M.A., 2000. Chemical Weathering, Atmospheric CO2, and Climate. Annu. Rev. Earth Planet. Sci. 28, 611–667.

Lal, D., 1991. Cosmic ray labeling of erosion surfaces: in situ nuclide production rates and erosion models. Earth Planet. Sci. Lett. 104, 424–439.

Lifton, N., Sato, T., Dunai, T.J., 2014. Scaling in situ cosmogenic nuclide production rates using analytical approximations to atmospheric cosmic-ray fluxes. Earth Planet. Sci. Lett. 386, 149–160. https://doi.org/10.1016/j.epsl.2013.10.052

Lomax, K.S., 2012. Business Failures : Another Example of the Analysis of Failure Data 1459.

Lukens, C.E., Riebe, C.S., Sklar, L.S., Shuster, D.L., 2016. Grain size bias in cosmogenic nuclide studies of stream sediment in steep terrain. https://doi.org/10.1002/2016JF003859.Received

Marrero, S.M., Phillips, F.M., Borchers, B., Lifton, N., Aumer, R., Balco, G., 2016. Cosmogenic nuclide systematics and the CRONUScalc program. Quat. Geochronol. 31, 160–187. https://doi.org/10.1016/j.quageo.2015.09.005

McPhillips, D., Bierman, P.R., Rood, D.H., 2014. Millennial-scale record of landslides in the Andes consistent with earthquake trigger. Nat. Geosci. 7, 925–930. https://doi.org/10.1038/ngeo2278

Niemi, N.A., Oskin, M., Burbank, D.W., Heimsath, A.M., Gabet, E.J., 2005. Effects of bedrock landslides on cosmogenically determined erosion rates. Earth Planet. Sci. Lett. 237, 480–498. https://doi.org/10.1016/j.epsl.2005.07.009

Page, M.T., Field, E.H., Milner, K.R., Powers, P.M., 2014. The UCERF3 Grand Inversion : Solving for the Long-Term Rate of Ruptures in a Fault System. Bull. Seismol. Soc. Am. 104, 1181–1204. https://doi.org/10.1785/0120130180

Phillips, F.M., Argento, D.C., Balco, G., Caffee, M.W., Clem, J., Dunai, T.J., Finkel, R., Goehring, B., Gosse, J.C., Hudson, A.M., Jull, A.J.T., Kelly, M.A., Kurz, M., Lal, D., Lifton, N., Marrero, S.M., Nishiizumi, K., Reedy, R.C., Schaefer, J., Stone, J.O.H., Swanson, T., Zreda, M.G., 2016. Quaternary Geochronology The CRONUS-Earth Project : A synthesis. Quat. Geochronol. 31, 119–154. https://doi.org/10.1016/j.quageo.2015.09.006

Riebe, C.S., Sklar, L.S., Lukens, C.E., Shuster, D.L., 2015. Climate and topography control the size and flux of sediment produced on steep mountain slopes. Proc. Natl. Acad. Sci. 112, 201503567. https://doi.org/10.1073/pnas.1503567112

Roering, J.J., Kirchner, J.W., Dietrich, W.E., 1999. Evidence for nonlinear, diffusive sediment transport on hillslopes and implications for landscape morphology. Water Resour. Res. 35, 853–870. https://doi.org/10.1029/1998WR900090

Rossi, M., Witt, A., Guzzetti, F., Malamud, B.D., Peruccacci, S., 2010. Analysis of historical landslide time series in the Emilia-Romagna region, northern Italy. Earth Surf. Process. Landforms 35, 1123–1137. https://doi.org/10.1002/esp.1858

Sazlvadori, G., 2002. Linear combinations of order statistics to estimate the position and scale parameters of the Generalized Pareto distribution. Stoch. Environ. Res. Risk Assess. 16. https://doi.org/10.1007/s00477-001-0080-2

Stone, J.O., 2000. Air pressure and cosmogenic isotope production. J. Geophys. Res. 105, 23753–23759.

Taylor, A., Blum, J.D., 1995. Relation between soil age and silicate weathering rates determined from the chemical evolution of a glacial chronosequence. Geology 23, 979–982. https://doi.org/10.1130/0091-7613(1995)023<0979:RBSAAS>2.3.CO

Van Der Woerd, J., Tapponnier, P., Ryerson, F.J., Mériaux, A., Meyer, B., Gaudemer, Y., Finkel, R.C., Caffee, M.W., Guoguang, Z., Zhiqin, X., 2002. Uniform postglacial slip-rate along the central 600 km of the Kunlun Fault (Tibet), from 26Al, 10Be, and 14C dating of riser offsets, and climatic origin of the regional morphology. Geophys. J. Int. 356–388.

West, A.J., Hetzel, R., Li, G., Jin, Z., Zhang, F., Hilton, R.G., Densmore, A.L., 2014. Dilution of 10Be in detrital quartz by earthquake-induced landslides: Implications for determining denudation rates and potential to provide insights into landslide sediment dynamics. Earth Planet. Sci. Lett. 396, 143–153. https://doi.org/10.1016/j.epsl.2014.03.058

Witt, A., Malamud, B.D., Rossi, M., Guzzetti, F., Peruccacci, S., 2010. Temporal correlations and clustering of landslides. Earth Surf. Process. Landforms 35, 1138–1156. https://doi.org/10.1002/esp.1998

Yanites, B.J., Tucker, G.E., Anderson, R.S., 2009. Numerical and analytical models of cosmogenic radionuclide dynamics in landslide-dominated drainage basins. J. Geophys. Res. Earth Surf. 114. https://doi.org/10.1029/2008JF001088

Zehfuss, P.H., Bierman, P.R., Gillespie, a. R., Burke, R.M., Caffee, M.W., 2001. Slip rates on the Fish Springs fault, Owens Valley, California, deduced from cosmogenic 10Be and 26Al and soil development on fan surfaces. Bull. Geol. Soc. Am. 113, 241–255. https://doi.org/10.1130/0016-7606(2001)113<0241:SROTFS>2.0.CO;2